

1 **Single-particle investigation of summertime and wintertime Antarctic sea spray aerosols**
2 **using low-Z particle EPMA, Raman microspectrometry, and ATR-FTIR imaging**
3 **techniques**

4
5 Hyo-Jin Eom¹, Dhruvajyoti Gupta¹, Hye-Rin Cho¹, HeeJin Hwang², SoonDo Hur², Yeontae Gim³
6 and Chul-Un Ro^{1,*}

7
8 ¹*Department of Chemistry, Inha University, Incheon, Republic of Korea*

9 ²*Polar Climate Change Research Division, Korea Polar Research Institute, Incheon, Republic of*
10 *Korea*

11 ³*Arctic Research Center, Korea Polar Research Institute, Incheon, Republic of Korea*

12
13 **ABSTRACT**

14 Two aerosol samples collected at King Sejong Korean scientific research station,
15 Antarctica on Dec. 9, 2011 in the austral summer (sample S1) and July 23, 2012 in the austral
16 winter (sample S2), when the oceanic chlorophyll-*a* levels on the collection days of the samples
17 were quite different, by ~19 times (2.46 vs. 0.13 μg/L, respectively), were investigated on a single
18 particle basis using quantitative energy-dispersive electron probe X-ray microanalysis (ED-
19 EPMA), called low-Z particle EPMA, Raman microspectrometry (RMS), and attenuated total
20 reflectance Fourier transform infrared (ATR-FTIR) imaging techniques to obtain their
21 characteristics based on the elemental chemical compositions, molecular species, and mixing state.
22 X-ray analysis showed that the supermicron summertime and wintertime Antarctic aerosol samples
23 have different elemental chemical compositions, even though all the individual particles analyzed
24 were sea spray aerosols (SSAs); i.e., the contents of C, O, Ca, S, and Si were more elevated,
25 whereas Cl was more depleted, for sample S1 than for sample S2. Based on qualitative analysis of
26 the chemical species present in individual SSAs by the combined application of RMS and ATR-
27 FTIR imaging, different organic species were observed in samples S1 and S2; i.e., Mg hydrate
28 salts of alanine were predominant in samples S1 and S2, whereas Mg salts of fatty acids internally

*Corresponding author. Tel.: +82 32 860 7676; fax: +82 32 874 9207
E-mail address: curo@inha.ac.kr (C.-U. Ro)

29 mixed with Mg hydrate salts of alanine were significant in sample S2. Although CaSO₄ was
30 observed significantly in both samples S1 and S2, other inorganic species, such as Na₂SO₄, NaNO₃,
31 Mg(NO₃)₂, SiO₂, and CH₃SO₃Mg, were observed more significantly in sample S1, suggesting that
32 those compounds may be related to the higher phytoplankton activity in summer.

33

34 INTRODUCTION

35 As more than 70% of the Earth's surface is covered by ocean, sea spray aerosols (SSAs)
36 make a dominant contribution to the total aerosol load in the air (Quinn et al., 2015). The influence
37 of nascent SSAs on the Earth's radiative balance, either directly by scattering light or indirectly by
38 acting as cloud droplets or ice nuclei, needs to be understood to better predict the additional
39 anthropogenic effects on SSAs (Ault et al., 2013a). Recently, it was suggested that SSAs mixed
40 with organic matter occurring at the ocean surface can have a significant influence on the Earth's
41 climate change (Wang et al., 2015). In addition, an understanding of the nascent SSA properties in
42 terms of the physical, chemical, and biological processes in the ocean surface is required to reduce
43 the current uncertainties for climate models (Prather et al., 2013).

44 SSAs are generated by bubbles bursting at the sea surface, where submicron and
45 supermicron SSAs are believed to be formed mostly from film drops and jet drops, respectively
46 (Quinn et al., 2014; Quinn et al., 2015; Wang et al., 2015). Submicron nascent SSAs were reported
47 to have more enriched organic species and less inorganic salts than the supermicron nascent SSAs
48 (Ault et al., 2013b; Prather et al., 2013; Wang et al., 2015). Although the molecular species of the
49 organic matter in nascent SSAs are unknown, a recent mesocosm experiment showed that
50 submicron SSAs were enriched with aliphatic-rich organic species, whereas supermicron SSAs
51 contained more oxidized organic species (Wang et al., 2015). As organic and inorganic matter in
52 sea water could be produced through the biological food web, the chemical compositions in
53 nascent SSAs would be interrelated with the biological activity in sea-water. On the other hand,
54 there have been disputes regarding the correlation between the biological activity in the ocean and
55 SSA organic matter in the marine boundary layer. Some studies reported positive correlations
56 between the levels of chlorophyll-*a*, which is an indicator of the biological activity in the sea-water,
57 and organic matter in SSAs (Prather et al., 2013; Hu et al., 2013; Rinaldi et al., 2010; O'Dowd et
58 al., 2004), whereas some showed no correlation between them (Quinn et al., 2014; Bates et al.,
59 2012). In addition, it was claimed that the chlorophyll-*a* level showed a complicated correlation

60 with the organic matters in nascent SSAs and the bacterial enzyme activities should also be
61 considered to better understand the overall generation and temporal variations of organic matter
62 (Wang et al., 2015), strongly suggesting the necessity for further studies.

63 The Antarctic region, which is isolated from anthropogenic sources, is one of the few
64 pristine places to study natural SSAs with a minimal anthropogenic influence (Maskey et al., 2011).
65 A major constituent in the Antarctic troposphere is nascent SSAs (Hara et al., 2012; Maskey et al.,
66 2011) and their chemical compositions can be altered through heterogeneous reactions with SO_4^{2-}
67 and CH_3SO_3^- during the summer (Hara et al., 2014). Some studies on the characterization and
68 seasonal cycles of different aerosol species at various Antarctic locations, such as McMurdo (Ross
69 Island), Aboa (Queen Maud Land), Syowa (East Ongul Island), Dome Fuji (Queen Maud Land),
70 O'Higgins (Chile), Admiralty Bay (King George Island), and Mizuho (Atka Bay) stations, have
71 been carried out, and bulk and single-particle analytical techniques showed that the sea-salts and
72 sulfur-containing species were the most abundant constituents in Antarctic aerosol samples (Hara
73 et al., 2013; Hara et al., 2012; Maskey et al., 2011; Préndez et al., 2009; Biancato et al., 2006;
74 Hara et al., 2006; Kerminen et al., 2000; Shaw, 1988). In this study, two Antarctic aerosol samples
75 collected on Dec. 9, 2011 in the austral summer (sample S1) and July 23, 2012 in the austral winter
76 (sample S2), having a drastic contrast in the oceanic chlorophyll-*a* levels on the collection days of
77 the samples, were characterized on a single particle basis using quantitative energy-dispersive
78 electron probe X-ray microanalysis (ED-EPMA), called low-*Z* particle EPMA, Raman
79 microspectrometry (RMS), and attenuated total reflection Fourier transform infrared (ATR-FTIR)
80 imaging. In the present study, low-*Z* particle EPMA was applied to investigate the elemental
81 compositional contrast between the summertime and wintertime samples and two vibrational
82 spectroscopic techniques, such as RMS and ATR-FTIR imaging, were employed on a single
83 particle basis to identify the organic and inorganic molecular species present in Antarctic aerosol
84 samples, clearly revealing the different chemical features between two samples.

85

86 **2. EXPERIMENTAL SECTION**

87 **2.1 Samples**

88 Aerosol samples were collected at a Korean scientific research station in the Antarctic: King
89 Sejong station ($62^\circ 13' \text{S}$, $58^\circ 47' \text{W}$), which is located at King George Island, Chile (see Figure S1
90 of the Supporting Information). King George Island in the South Ocean is 120 km off the coast of

91 Antarctica, and is dominated by pervasive ice caps, with more than 90% of the island being
92 glaciated. This study examined two aerosol samples S1 and S2 collected on Dec. 9, 2011 in the
93 austral summer and July 23, 2012 in the austral winter, respectively, when the oceanic chlorophyll-
94 *a* levels on the collection days of the samples were quite different, by ~19 times (2.46 vs. 0.13
95 $\mu\text{g/L}$, respectively). The oceanic chlorophyll-*a* levels for water samples collected daily from
96 nearby oceanic water were determined using a fluorometer (TD 700, Turner Design, USA)). The
97 detailed description for chlorophyll-*a* determination is given elsewhere (Schloss et al., 2014; Lee
98 et al., 2015). The aerosol samples were collected on Al foil substrates (Sigma-Aldrich, 99.8%
99 purity) using a three stage cascade impactor (PM_{10} Impactor, Dekati Inc.) during daytime at
100 temperatures, $T = 1.1 - 2.1$ °C and $-1.9 - -1.5$ °C and relative humidity, $\text{RH} = 94.1 - 94.5$ % and
101 $87.6 - 92.1$ % for samples S1 and S2, respectively. The impactor had aerodynamic cut-sizes of 10,
102 2.5, and 1 μm for stages 1, 2, and 3, respectively, at a 10 L min^{-1} sampling flow, and individual
103 particles collected on stages 2 and 3 ($\text{PM}_{2.5-10}$ and $\text{PM}_{1.0-2.5}$ fractions with the size range of 2.5–10
104 μm and 1–2.5 μm , respectively) were examined.

105 Three-day (72 h) backward air-mass trajectories were obtained using the Hybrid
106 Lagrangian Single-Particle Integrated Trajectory (HYSPLIT) model from the NOAA Air
107 Resources Laboratory's web server (<http://www.arl.noaa.gov/ready/hysplit4.html>). The back-
108 trajectories for samples S1 and S2 show that the air-masses at heights of 500 m, 1000 m, and 1500
109 m above sea level, which originated from the Pacific Ocean, travelled over the Pacific Ocean and
110 passed over Chile, respectively (see Figure S1 of the Supporting Information).

111

112 **2.2 Low-Z particle EPMA measurement and data analysis**

113 Low-Z particle EPMA measurements were carried out by scanning electron microscopy
114 (JSM-6390, JEOL) equipped with an Oxford Link SATW ultrathin window energy-dispersive X-
115 ray (EDX) detector, which has a spectral resolution of 133 eV for Mn $\text{K}\alpha$ X-rays. The X-ray spectra
116 and elemental X-ray maps were recorded using INCA Energy software. An accelerating voltage
117 of 10 kV and a beam current of 0.5 nA, and a typical measuring time of 20 s were used for the X-
118 ray spectral data acquisition using area mode, where the X-ray signals were obtained by the
119 scanning electron beam over the entire area of each particle. The net X-ray intensities for the
120 chemical elements were obtained by a non-linear, least-square fit of the spectra collected using the
121 AXIL program (Vekemans et al., 1994). The elemental concentrations of the individual particles

122 were determined from their X-ray intensities using a Monte Carlo calculation combined with
123 reverse successive approximations (Ro et al., 2003). For the X-ray mapping measurements, an
124 accelerating voltage and beam current are the same as the area mode measurements except for a
125 typical measuring time of 30 min. A more detailed discussion of the EPMA measurement
126 conditions can be found elsewhere (Ro et al., 2005; Ro et al., 1999).

127

128 **2.3 RMS measurements**

129 The particles collected on Al foil were mounted on the microscope stage of a confocal
130 Raman microspectrometer (XploRA, Horiba Jobin Yvon) equipped with a 100×, 0.9 numerical
131 aperture objective (Olympus). Raman point and mapping measurements were carried out under
132 ambient conditions. Optical images of the particles for relocation were obtained using a video
133 camera. Raman scattering was excited at the 532 nm wavelength using an air-cooled diode laser
134 and detected with a multichannel air cooled charge-coupled device (CCD) at an 1800 gr/mm
135 grating. The excitation laser power delivered to the individual particles was approximately 3 mW
136 using a controlled confocal hole of 300 ~ 500 μm and a slit, 100 μm in diameter. The spectral
137 ranges of 100–4000 cm⁻¹ were performed with a 5 s acquisition time and 5 times accumulation for
138 each measurement. The spectral resolution was 1.8 cm⁻¹ and the spot size of the laser beam at the
139 sample was estimated to be ~1 μm². The XYZ computer-controlled Raman mapping was
140 performed by obtaining the Raman spectra in point-by-point XY scanning mode with a 1 μm step
141 and a 5 s integration time per pixel. The spectra and images were acquired using Labspec6 software.
142 A more detailed discussion of the RMS measurement conditions for single particle analysis can be
143 found elsewhere (Sobanska et al., 2012; Eom et al., 2013; Jung et al., 2014).

144

145 **2.4 ATR-FTIR imaging measurements**

146 The ATR-FTIR imaging measurements were performed using a Perkin Elmer Spectrum
147 100 FTIR spectrometer interfaced to a Spectrum Spotlight 400 FTIR microscope. An ATR
148 accessory using a germanium hemispherical IRE crystal, 600 μm in diameter, was used for ATR
149 imaging. The ATR accessory was mounted on the X–Y stage of the FTIR microscope and the IRE
150 crystal was made to come into contact with the sample through a force lever. A spatial resolution
151 of 3.1 μm at 1726 cm⁻¹ ($\lambda = 5.79 \mu\text{m}$) is achievable (Van Dalen et al., 2007). A 16 x 1 pixel mercury
152 cadmium telluride (MCT) array detector was used to obtain the FTIR images with a pixel size of

153 1.56 μm . For each pixel, an ATR-FTIR spectrum, ranging from 680 to 4000 cm^{-1} with a spectral
154 resolution of 4 cm^{-1} , was obtained from eight interferograms, which were co-added and Fourier-
155 transformed. The position of the crystal on the sample was determined using an optical microscope
156 equipped with a light emitting diode and a CCD camera, which allowed relocation of the same
157 single particles that had been analyzed using RMS before ATR-FTIR imaging. Spectral data
158 processing was performed using Perkin Elmer Spectrum IMAGE software. A more detailed
159 discussion of the ATR-FTIR imaging measurement conditions for single particle analysis can be
160 found elsewhere (Song et al., 2010; Song et al., 2013; Jung et al., 2014).

161

162 **3. RESULTS AND DISCUSSION**

163

164 **3.1 Single-particle characterization of the summertime and wintertime Antarctic SSAs** 165 **using low-Z particle EPMA**

166

167 Figure 1 presents typical secondary electron images (SEIs) of the individual particles on
168 two $\text{PM}_{2.5-10}$ (stage 2) samples collected in the austral summer and winter, where the chemical
169 species comprising each particle, determined from X-ray spectral data, is indicated. All the
170 particles on the images are of a marine origin having major Na and Cl contents with small
171 quantities of C, O, Mg, K, Ca, S, and/or Si. Overall, approximately 600 particles of samples S1
172 and S2 examined by low-Z particle EPMA were of a marine origin. Na, Mg, Cl, S, C, and O were
173 present in all the particles, whereas K, Ca, and Si were observed more frequently in the
174 summertime sample S1 than in the wintertime sample S2 (93.6 % vs. 79.4 % relative encountering
175 frequencies for K; 93.9 % vs. 75.5 % for Ca; and 70.1 % vs. 0.7 % for Si, respectively, where the
176 relative encountering frequency (in %) for a certain element is defined as the number of particles
177 containing the element divided by the total number of particles analyzed for a sample.). In
178 particular, Si is present exclusively in sample S1, which might be a good indicator of the
179 phytoplankton influence on the nascent SSAs.

180 As ambient relative humidity (RH) at the sampling times were higher than 87.6% and the
181 efflorescence RHs (ERHs) of the inorganic sea salt components (e.g., ERHs of NaCl and CaSO_4
182 are ~45-47 % and ~80-90 %, respectively (Gupta et al., 2015; Schindelholz et al., 2014; Xiao et
183 al., 2008)), the SSAs would be collected as aqueous droplets at the time of collection. Once

184 exposed at a low RH, e.g. by being either handled under the dry ambient conditions or placed in
185 the vacuum chamber of SEM, they would crystallize fractionally, resulting in their heterogeneous
186 mixing states, as shown in Figure 1, having bright and crystalline solids, segregated and somewhat
187 dark regions, and elongated rods (indicated by the yellow arrows in Figure 1), which are more
188 distinctive for the summertime particles. The fractional crystallization of SSAs has also been
189 reported (Ault et al., 2013a; Hara et al., 2013; Hara et al., 2014). To determine the chemical species
190 of the crystalline solids, dark regions, and rods, elemental X-ray and molecular Raman mapping
191 measurements were performed on the same individual SSA particles. Figure 2 presents the SEIs
192 and molecular Raman and elemental X-ray map images of two typical summertime and wintertime
193 SSA particles. As Raman-inactive NaCl and MgCl₂ species cannot generate Raman signals, Raman
194 mapping was performed to determine the spatial distributions of CaSO₄ (using Raman signal in
195 1000 – 1020 cm⁻¹ range), Na₂SO₄ (using Raman signal in 985 – 995 cm⁻¹ range), and organic
196 species (using Raman signal in 2800 – 3000 cm⁻¹ range). X-ray mapping images of Na, Mg, Ca,
197 Cl, S, C, and O are overlaid in different colors on the SEIs. Molecular Raman images look broader
198 than elemental X-ray images as the spatial resolution of Raman mapping (~1 μm) is larger than
199 that of X-ray mapping (~0.1 μm). Especially, Raman images for organic species look more spread
200 than C X-ray map images as the low energy C X-rays generated from underneath are not often
201 detected due to the strong absorption by solid particles sitting above. Nonetheless, the combined
202 Raman and X-ray map image data of Figure 2(a) clearly indicate that the upper bright solid (region
203 1, notated on the SEI of Figure 2(a)) of the summertime SSA particle is composed of NaCl, the
204 bottom-right region 3 is a mixture of MgCl₂ and organic species (having a somewhat dark
205 appearance due to the low secondary electron yield of organic species), and the two elongated rods
206 are of a mixture of CaSO₄ and Na₂SO₄. The wintertime SSA particle in Figure 2(b) is composed
207 of NaCl (at region 1) and the mixture of MgCl₂ and organic species (at region 2). As C and O are
208 overlapping in their X-ray maps of Figure 2, the organic species appear to contain a significant
209 amount of oxygen. Figure 3 shows the X-ray spectra and elemental atomic concentrations obtained
210 from the entire regions of the summertime and wintertime particles using area-mode X-ray data
211 acquisition. The summertime particle contains more C, O, Si, S, and Ca than the wintertime particle.
212 As the amount of sulfate (by assuming all the sulfur exists as sulfate) for the summertime particle
213 is larger than that of Ca, the sulfate first crystallized as CaSO₄, and the remaining sulfate
214 crystallized as Na₂SO₄, resulting in the formation of elongated rods composed of a mixture of

215 CaSO₄ and Na₂SO₄. For the wintertime particle, CaSO₄ was observed weakly at the upper-right
216 region because of the low sulfate content.

217 Table S1 in the Supporting Information shows the mean elemental concentrations for an
218 overall ~600 individual particles in PM_{1.0-2.5} and PM_{2.5-10} fractions of the summertime and
219 wintertime samples, obtained by low-Z particle EPMA. As all the particles analyzed in these
220 samples are of a marine origin, the mean atomic concentrations of Na and Cl are largest (ranging
221 in 25.2 – 28.3 % and 24.8 – 29.2 %, respectively), followed by high C and O concentrations (18.8
222 – 27.1 % and 17.3 – 19.5 %, respectively), compared to those of Mg, Si, S, K, and Ca which are
223 in the range, 0.0 – 2.9 %. Based on the mean elemental weight concentrations, the C and O contents
224 were smaller based on the mean atomic concentrations, even though they were still considerable
225 (9.6 – 14.6 % and 12.0 – 13.6 %, respectively). On the other hand, the organic contents on a
226 molecular basis would be smaller than the elemental C contents but the molecular organic content
227 could not be estimated because the organic molecular species in SSAs have not been identified
228 clearly (Ault et al., 2013b; Laskina, 2015; Quinn et al., 2015). An interesting observation was that
229 all the supermicron Antarctic SSAs both in the summertime and wintertime samples were a
230 mixture of inorganic and organic species.

231 To better examine the chemical compositional contrast between samples S1 and S2, Table
232 1 lists the mean elemental concentration ratios to Na for individual particles together with those
233 for bulk sea-water. The atomic concentration ratios of C, O, Si, S, and Ca; Cl; and Mg and K for
234 the summertime sample were higher and lower than and similar to those of the wintertime sample,
235 respectively (also see Fig. S2, which clearly shows different distributions of individual particles
236 having specific elemental concentration ratios between the summertime and wintertime samples),
237 indicating that C, O, Si, S, and Ca; and Cl are enriched and depleted in the summertime sample,
238 respectively. In addition, those enriched and depleted elements have higher and lower
239 concentration ratios than the bulk sea-water ratios, respectively.

240 As the [C]/[Na] ratios for both samples were high compared to bulk sea-water [C]/[Na]
241 ratio, even the supermicron Antarctic SSAs contain significantly enriched organic species. The
242 [C]/[Na] ratios of sample S1 were higher than those of sample S2, suggesting that the higher
243 organic matter is related to the higher phytoplankton activities, and those for particles in the PM<sub>1.0-
244 2.5</sub> fractions of samples S1 and S2 (1.12 and 0.83, respectively) were higher than PM_{2.5-10} fractions
245 (0.87 and 0.70, respectively), indicating that the smaller particles contain more organic species,

246 which is consistent with other observations reporting more organics in the smaller SSAs (Quinn et
247 al., 2015).

248 The [O]/[Na] ratios of sample S1 are higher than those of sample S2, and those for particles
249 in the $PM_{2.5-10}$ fractions of samples S1 and S2 (0.77 and 0.68, respectively) are higher than the
250 $PM_{1.0-2.5}$ fractions (0.71 and 0.66, respectively). Similar observations were made for S and Ca, for
251 which the elemental concentration ratios were somewhat higher in sample S1 and in larger size
252 fractions (see Table 1). In addition, the frequencies of encountering particles having higher [S]/[Na]
253 or [Ca]/[Na] ratios than bulk sea-water were significantly higher in the summertime sample and in
254 the larger size fractions (see encountering frequency data for S and Ca in Table 1), indicating that
255 O, S, and Ca are interrelated with common sources, which is also supported by the observation of
256 elongated $CaSO_4$ rods in the Raman and X-ray mapping measurements. The enriched S and O in
257 the S1 sample appear to be due to the elevated $nss-SO_4^{2-}$ levels. In the austral summer
258 (November–March) of the Antarctic, higher solar radiation levels and temperatures than the other
259 seasons tend to enhance the phytoplankton activities (as supported by its high chlorophyll-*a* level
260 for sample S1), which enhances the production and emission of oceanic dimethyl sulfide (DMS)
261 (Wagenbach et al., 1998; Preunkert et al., 2008). The volatile DMS in the atmosphere undergoes
262 complex sequences of gas-phase oxidation reactions, generating a range of sulfur-containing
263 products, such as dimethyl sulfoxide (DMSO), methanesulfonic acid (MSA), SO_2 , and H_2SO_4
264 (Gaston et al., 2010). These oxidized products can condense onto preexisting particles, resulting
265 in the formation of $nss-SO_4^{2-}$ -containing SSAs. As $CaSO_4$ can efflorescence at very high RH, the
266 $nss-SO_4^{2-}$ can combine easily with Ca, as observed in Figure 1, where the $CaSO_4$ rods are observed
267 more frequently in sample S1.

268 Si is observed for the summertime particles, and more abundantly ([Si]/[Na] = 0.03 vs.
269 0.01) and frequently (encountering frequency = 93.4 % vs. 47.5 %) in the $PM_{1.0-2.5}$ fraction than in
270 the $PM_{2.5-10}$ fraction. As Si is observed mostly in sample S1 and more in the smaller size fraction,
271 it appears to be from fragments of silica cell walls of diatoms, a major group of algae and a
272 common type of phytoplankton in the oceans (Litchman and Klausmeier, 2008; Alpert et al., 2015).
273 In the winter, the reduced diatom activities would decrease the emission of Si species into the
274 atmosphere, resulting in the scarce observation of Si in the S2 sample.

275 In the SSAs of samples S1 and S2, only Cl is depleted compared to bulk sea-water ([Cl]/[Na]
276 = 1.00 and 1.03 for samples S1 and S2, respectively, vs. 1.16 for sea-water), and the Cl depletion

277 is somewhat higher for the summertime SSAs than the wintertime and for $PM_{1.0-2.5}$ fractions than
278 $PM_{2.5-10}$ fractions, suggesting that Cl was liberated by the reactions of NaCl and/or $MgCl_2$ with
279 $nss-SO_4^{2-}$ and/or $CH_3SO_3^-$, which are more abundant in the summer, with more depletion for
280 smaller SSAs having a higher surface to volume ratio and higher reactivity.

281

282 **3.2 Single-particle molecular speciation of Antarctic SSAs using RMS and ATR-FTIR** 283 **imaging**

284

285 Based on low-Z particle EPMA analysis, the C, O, Si, S, and Ca levels were elevated for
286 the summertime SSAs on a single-particle basis. This quantitative elemental X-ray analysis
287 provides useful information on their morphology, elemental chemical compositions, and mixing
288 states of individual Antarctica SSAs. On the other hand, as low-Z particle EPMA has a limitation
289 on molecular speciation and hydrogen detection, the RMS and ATR-FTIR imaging techniques
290 were applied in combination for the analysis of the same individual SSAs to investigate their
291 Raman- and IR-active organic and inorganic molecular species. Raman and ATR-FTIR techniques
292 are useful because their spectra of organic and inorganic compounds are quite specific depending
293 on their chemical species, phase, crystallinity, and neighboring environment. In particular, the
294 complicated vibrational spectral patterns observed in the fingerprint region ($< 1500\text{ cm}^{-1}$) in the
295 Raman and FTIR spectra can be critically useful for the positive or negative identification of
296 specific organic compounds with the same phase and crystallinity. In addition, the differences in
297 their spectra owing to their different signal generation mechanisms (i.e., scattering vs. absorption
298 of energy) and different selection rules would make the two fingerprint techniques rather
299 complementary (Jung et al., 2014).

300

301 **3.2.1 Organic species**

302 Among the ~250 individual SSAs of samples S1 and S2 investigated by RMS and ATR-
303 FTIR imaging techniques, the frequently observed organic species are most probably ones
304 containing Mg hydrate salts of alanine (MgAla) and Mg salts of fatty acids (MgFAs).

305 Figure 4 shows baseline-corrected Raman and ATR-FTIR spectra of two individual
306 summertime SSAs containing mainly two types of MgAla (detailed identification is given later.)
307 with some inorganic compounds. If several peaks from inorganic compounds (i.e., Raman peaks

308 at 124 and 467 cm^{-1} for SiO_2 , at 717 and 1052 cm^{-1} for $\text{Mg}(\text{NO}_3)_2$, at 989 cm^{-1} for Na_2SO_4 , at 1008
309 cm^{-1} for $\text{CaSO}_4 \cdot 2\text{H}_2\text{O}$, and at 1068 cm^{-1} for NaNO_3 ; and ATR-FTIR peaks at 1087 and 1165 cm^{-1}
310 for SiO_2 , at 1100 cm^{-1} for Na_2SO_4 and $\text{CaSO}_4 \cdot 2\text{H}_2\text{O}$) are excluded from the consideration, the
311 Raman and ATR-FTIR spectra of two types of SSAs are similar except for their different Raman
312 and ATR-FTIR peak shapes. That is, the Raman peaks of crystalline water are sharp at 3276 and
313 3390 cm^{-1} for Type 1 SSA, compared to the relatively broad peak at 3410 cm^{-1} for Type 2 SSA.
314 The C-H vibration Raman peaks of Type 1 SSA are split at 3000/2988 cm^{-1} and 2940/2919 cm^{-1} ,
315 which correspond to the non-split Raman peaks of Type 2 SSA at 2989 cm^{-1} and 2939 cm^{-1} . The
316 C-H bending Raman peaks of Type 1 SSA are split into 1433/1457/1479 cm^{-1} , which correspond
317 to the Raman peaks of Type 2 SSA at 1427/1452 cm^{-1} . In the fingerprint region, the characteristic
318 Raman peaks both for Types 1 and 2 SSAs are observed at 869, 1102, 1130, 1254, ~1300, ~1370,
319 and 1640 cm^{-1} . Similarly, the ATR-FTIR peaks of crystal water are sharp and broad at 3265 and
320 3370 cm^{-1} for Type 1 SSA and 3372 cm^{-1} for Type 2 SSA, respectively, even though the C-H
321 vibration ATR-FTIR peaks are unclear for both types of SSAs. In the ATR-FTIR spectra, the water
322 bending peaks at ~1640 cm^{-1} are quite strong for both Types SSAs with the peak of Type 1 SSA
323 being much sharper. In the fingerprint region, the characteristic ATR-FTIR peaks for both Types 1
324 and 2 SSAs at 770, 869, 1127, 1254, 1312, ~1360, 1376, 1428, 1476, and 1507 cm^{-1} were sharp
325 and broad for the Type 1 and Type 2 SSAs, respectively. Similar Raman and ATR-FTIR peak
326 patterns of the Types 1 and 2 spectra except for their different peak shapes strongly indicates that
327 they have the same in chemical compositions but with different crystal structures. As amorphous
328 solids tend to provide broader Raman and ATR-FTIR peaks than crystalline solids (Shebanova and
329 Lazor, 2003; Gouadec and Colombari, 2007; Lutz and Haeuseler, 1999; Yan et al., 2008), the Types
330 1 and 2 SSAs are most likely amorphous and crystalline solid particles, respectively.

331 Figure S3 shows the Raman and ATR-FTIR spectra of aerosols generated by the
332 nebulization of a mixture solution of 0.2 M alanine and 0.1 M MgCl_2 standard chemicals and
333 collected on Al foil. All the fresh aerosol particles immediately after nebulization showed the first
334 pair of Raman and ATR-FTIR spectra in Figure S3 on a single particle basis, which resemble the
335 Raman and ATR-FTIR spectra shown in Figure 4(b) when the Raman and ATR-FTIR peaks from
336 the inorganic compounds are excluded. In particular, the ATR-FTIR spectra in Figure 4(b) and
337 Figure S3 appear similar. When the aerosols were measured ~1 year later after the generated
338 aerosols had been sealed in a plastic box and stored in a desiccator, approximately half of the

339 generated aerosols showed a second pair of Raman and ATR-FTIR spectra, as shown in Figure S3,
340 and the other half showed a third pair. The third spectra pair appears similar to those in Figure 4(a)
341 for a crystalline solid SSA, whereas the second spectra pair appears to be between the first and
342 third spectra pairs in Figure S3, strongly suggesting that the fresh aerosols generated from the
343 alanine and MgCl₂ solution are a somewhat amorphous form of MgAla, whereas the second and
344 third spectra pairs suggest a more crystalline nature of MgAla. The Raman peaks of the aerosols
345 generated at 3409 and 1637 cm⁻¹ are not from free water because these Raman peaks were
346 unchanged even at very low RH (< 5%) when the in-situ Raman measurement was performed by
347 changing the RH in the hygroscopic measurement system described in a previous study (Gupta et
348 al., 2015). This means that the intensities and shapes of the Raman peaks should be reduced and
349 changed, respectively, when the RH is decreased to a very low level if these peaks are from free
350 water. In other words, the peaks are from the hydrate crystal water bound for divalent Mg
351 compounds as the narrow peak shapes and peak positions resemble those of the known spectra of
352 MgCl₂·6H₂O and MgCl₂·4H₂O solids with hydrate crystal water (Gupta et al., 2015). Divalent Ca
353 ions are also present in sea-water. However, based on X-ray and Raman mapping results, Ca ions
354 are mostly combined with inorganic SO₄²⁻ and slightly present in regions where organic moieties
355 are.

356 Based on a comparison of the Raman and ATR-FTIR spectra obtained for the summertime
357 SSAs and aerosols generated from the mixture solution of standard alanine and MgCl₂, the organic
358 species are ones containing mainly the Mg hydrate salts of alanine (MgAla), even though their
359 precise molecular formula and the other possible minor components could not be confirmed. The
360 Raman spectrum, which is the same as that of crystalline MgAla, was also observed for nascent
361 SSAs produced using breaking waves, even though their molecular species were not identified
362 (Ault et al., 2013b; Wang et al., 2015). In a previous study, the ATR-FTIR spectra were obtained
363 from other summertime Antarctica SSAs, which appear very similar to that of amorphous MgAla
364 (Maskey et al., 2011). Interestingly, almost all the ATR-FTIR spectra obtained in the previous work
365 were for amorphous MgAla, whereas among the 254 individual SSAs analyzed in this study, the
366 number of crystalline and amorphous MgAla-containing SSAs were 246 and 8, respectively, based
367 on their Raman and ATR-FTIR spectra. How crystallization from SSAs occurred to form these
368 organic Mg hydrate salts in the Antarctic environment is unclear because crystalline salts could
369 not be made under very dry conditions and by oven-drying overnight. On the other hand, somewhat

370 crystalline salts were encountered from the generated aerosol sample stored for ~ 1 year in a
371 desiccator. Some efficient efflorescence seeds should be present in the Antarctic SSAs, which have
372 much more complicated chemical compositions than the mixture solution of pure alanine and
373 MgCl₂. The identification of an accurate molecular formula and structure of MgAla and an
374 investigation of the crystallization mechanism requires further study.

375 The dominant dissolved amino acid in sea-water is glycine followed by alanine, aspartic
376 acid or serine (Ogawa and Tanoue, 2003; Dittmar et al., 2001). In sea-water, MgAla species would
377 be present as dissolved organic matter (DOM) in the form of alanine before being airborne. On the
378 other hand, based on the Raman and ATR-FTIR spectra of standard powdery glycine and aerosol
379 particles nebulized from aqueous mixtures of glycine/MgCl₂ and glycine/alanine/MgCl₂ as well as
380 other common target chemicals for organic matter in nascent SSAs such as sodium dodecyl sulfate,
381 a dipeptide of alanine and glycine, a polypeptide, and lipopolysaccharides, which are shown in
382 Figure S4, it is clear that MgAla-containing SSAs are composed of mainly alanine with negligible
383 glycine and other target chemicals. As the Raman and ATR-FTIR sensitivities for alanine and
384 glycine are comparable and the same Raman spectrum for MgAla was also observed in the nascent
385 SSAs produced from breaking waves, there must be some unknown processes for the generation
386 of MgAla-containing SSAs from sea-water.

387 Figure 5 shows the baseline-corrected Raman and ATR-FTIR spectra of two individual
388 SSAs of sample S2 containing mainly MgFAs and both MgAla and MgFAs. As shown in Figure
389 S5, the Raman spectra of powdery standard Mg palmitate, palmitic acid, Mg stearate, and stearic
390 acid appear similar except for minor differences in relative peak intensities, which is not sufficient
391 to identify the organic species having the Raman spectrum of Figure 5(a). On the other hand, Mg
392 palmitate/stearate and palmitic/stearic acids have very different ATR-FTIR spectra as shown in
393 Figure S5. Owing to their additional strong peaks at ~1700 cm⁻¹ for the -COOH functional group
394 and very different peak patterns in the fingerprint region of 700 – 1600 cm⁻¹, palmitic/stearic acids
395 can be clearly distinguishable from Mg palmitate/stearate. The ATR-FTIR spectrum of Mg
396 palmitate is different from that of Mg stearate based on the strong hydrate peaks at 3374 and 3256
397 cm⁻¹ for Mg palmitate and the clearly different peak patterns in the wavenumber range, 1200 -
398 1600 cm⁻¹, between those of Mg palmitate and stearate. Figure S6 shows the ATR-FTIR spectra of
399 Mg palmitate, Mg stearate, a mixture of Mg palmitate and stearate (by 3:1), and MgFAs-containing
400 SSA, where the spectra of the mixture particle and the SSA match quite well, indicating that the

401 exemplar Antarctic SSA is a mixture of Mg palmitate and stearate. Therefore, this type of SSA is
402 called the Mg salts of fatty acids (MgFAs) above. The same Raman spectrum as that of MgFAs
403 was also observed for the nascent SSAs produced using breaking waves (Ault et al., 2013b; Wang
404 et al., 2015). As the pKa of palmitic and steric acids is 4.95, the palmitic/stearic acid moieties
405 degraded from the lipids would exist predominantly as surfactant palmitate/stearate in SSML
406 and/or on sea-surface and would crystallize as their Mg salts after the MgFAs-containing SSAs
407 were airborne by bubble busting.

408

409 **3.2.2 Inorganic species**

410

411 The Raman and IR active inorganic species observed in the Antarctic SSAs were CaSO_4 ,
412 Na_2SO_4 , NaNO_3 , $\text{Mg}(\text{NO}_3)_2$, NH_4NO_3 , $\text{CH}_3\text{SO}_3\text{Mg}$ (Mg methanesulfonate), and SiO_2 and their
413 standard Raman and ATR-FTIR spectra are shown in Figure S7. The inorganic species present in
414 the SSAs could be identified clearly by matching both the Raman and ATR-FTIR spectra of the
415 SSAs with those of the standard inorganic compounds, even though the inorganic species in the
416 SSAs were observed together with organic species so that the Raman and ATR-FTIR peaks of
417 inorganic species sometimes appear weak compared to those of organic species. On the other hand,
418 even under that situation, RMS is a powerful tool as the Raman peaks of inorganic compounds are
419 quite useful for identifying them.

420

421 **3.3 Single-particle characterization of Antarctic SSAs using RMS and ATR-FTIR imaging**

422

423 Table 2 shows relative encountering frequencies of the organic and inorganic species for
424 ~250 individual Antarctic SSAs. The encountering frequency of certain chemical species was
425 determined by counting the number of individual SSAs containing the species, regardless of its
426 content as the Raman and ATR-FTIR spectral data were used for qualitative molecular speciation.
427 Based on X-ray analysis, C and O were present in all the analyzed Antarctic SSAs. Indeed, organic
428 salt species were detected for all the particles of samples S1 and S2, showing that organic species
429 are ubiquitously present, even in supermicron SSAs. As shown in Table 2, organic salt species
430 were categorized into three groups containing (i) MgAla, (ii) MgFAs, and (iii) mixtures of the two
431 organic salts. The Raman and IR active inorganic salts were always observed together with organic

432 salt species, so that the relative encountering frequencies of inorganic species are shown in each
433 organic group.

434 All the particles of sample S1 contained only MgAla together with other inorganic species.
435 In particular, CaSO₄ and Na₂SO₄ are mixed almost internally with MgAla (for PM_{1.0-2.5} and PM_{2.5-}
436 ₁₀ fractions, the encountering frequencies of CaSO₄ were 98.3% and 92.9%, respectively, and those
437 of Na₂SO₄ were 98.3% and 88.6%, respectively), indicating that SO₄²⁻ is mostly in the form of a
438 CaSO₄ and Na₂SO₄ mixture. Although N X-ray signal was not detected probably due to the small
439 amount of NO₃⁻ present in the Antarctic SSAs, Mg(NO₃)₂ and NaNO₃ were frequently observed
440 in samples S1 and S2 using Raman and ATR-FTIR techniques. The nitrate in sea-water can be
441 generated by the photoammonification process, which transforms dissolved organic nitrogen
442 (DON) to labile inorganic nitrogen, mainly ammonium (NH₄⁺) (Kitidis et al., 2006; Aarnos et al.,
443 2012; Xie et al., 2012; Rain-Franco et al., 2014; Paulot et al., 2015), followed by the microbial
444 oxidation of ammonium into nitrate (NO₃⁻) by nitrifying bacteria (Carlucci et al., 1970; Hovanec
445 and Delong, 1996; Smith et al., 2014; Tolar et al., 2016). As the photoammonification depends on
446 solar radiations, the ammonium and nitrate production would be enhanced in the summer with
447 higher solar radiation level. Indeed, as shown in Table 2, nitrates are more frequently observed in
448 summertime sample S1 than wintertime sample S2. For the PM_{1.0-2.5} and PM_{2.5-10} fractions of
449 sample S1, the overall encountering frequencies of Mg(NO₃)₂ are 51.7% and 77.1%, respectively,
450 and those of NaNO₃ were 0.0% and 38.6%, respectively, where the NO₃⁻ moiety was observed
451 more in the PM_{2.5-10} fraction. The reason for why the NO₃⁻ moiety is more abundant in the PM_{2.5-}
452 ₁₀ fraction is unclear. The SiO₂ concentration was 46.6% and 27.1% in the PM_{1.0-2.5} and PM_{2.5-10}
453 fractions, respectively. SiO₂, which would be from fragments of silica cell walls of diatoms,
454 appears to be in colloidal form because SiO₂ species are not water-soluble and were observed more
455 in the PM_{1.0-2.5} fraction than in PM_{2.5-10}. A small number of Mg methanesulfonate was observed
456 only in the PM_{1.0-2.5} fraction of sample S1. Higher phytoplankton activities in the summer enhance
457 the production and emission of oceanic DMS, resulting in the production of MSA, which is a
458 strong acid that can exist as an anion in sea-water and is observed as Mg salts in SSAs, even though
459 its encountering frequency is not high compared to other sulfates.

460 A significant portion of SSAs of sample S2 contain only MgAla (overall 76.6% and 33.9%
461 for PM_{1.0-2.5} and PM_{2.5-10} fractions, respectively) (see Table 2). Considering the encountering
462 frequencies of MgAla mixed with MgFAs (21.9% and 54.8% for PM_{1.0-2.5} and PM_{2.5-10} fractions,

463 respectively), MgAla is also almost ubiquitous in sample S2 (overall 98.5% and 88.7% for PM_{1.0-}
464 _{2.5} and PM_{2.5-10} fractions, respectively). MgFAs mixed internally with MgAla was encountered
465 significantly in sample S2 (overall 23.5% and 66.1% for PM_{1.0-2.5} and PM_{2.5-10} fractions,
466 respectively). For the PM_{1.0-2.5} and PM_{2.5-10} fractions, the encountering frequencies of CaSO₄ were
467 98.5% and 88.6% overall, respectively, whereas those of Na₂SO₄ were 26.6% and 8.0%,
468 respectively, indicating that SO₄²⁻ is mostly in the form of CaSO₄. For the PM_{1.0-2.5} and PM_{2.5-10}
469 fractions, the overall encountering frequencies of Mg(NO₃)₂ were 43.8% and 75.8%, respectively,
470 and those of NaNO₃ were 12.5% and 27.4%, respectively, where the NO₃⁻ moiety was also
471 observed more in the PM_{2.5-10} fraction. SiO₂ was encountered much less frequently, 7.9% and 3.2%
472 in the PM_{1.0-2.5} and PM_{2.5-10} fractions, respectively, compared to those of sample S1 (i.e., 46.6%
473 and 27.1%, respectively). The observation of a higher encountering frequency of SiO₂ in sample
474 S1 is consistent with that of X-ray analysis, where the detection of the Si X-ray signal was 70.1 %
475 and 0.7 % for samples S1 and S2, respectively.

476 The relative encountering frequency data for the organic and inorganic species of samples
477 S1 and S2 clearly show their different chemical compositional features. MgAla-containing SSAs
478 are predominant for samples S1 and S2. The MgFAs were not observed in sample S1, but were
479 observed in sample S2, mostly as internal mixtures with MgAla. As alanine is water-soluble and
480 anions of fatty acids are surfactants, they would be present mostly at the bulk sea-water and
481 SSML/sea-surface, respectively, before becoming airborne. Therefore, alanine- and fatty acids-
482 containing SSAs are expected to be airborne through jet- and film-drop production during bubble
483 busting, resulting in the generation of supermicron and submicron SSAs, respectively (de Leeuw
484 et al., 2011; Quinn et al., 2015). In this study, supermicron SSAs were investigated for which
485 MgAla is almost ubiquitous in samples S1 and S2, indicating that the supermicron SSAs were
486 generated as jet-drops. As MgFAs was observed mostly together with MgAla in sample S2, the
487 MgFAs-containing SSAs originating from film-drops might agglomerate with MgAla-containing
488 supermicron SSAs in the air.

489 In a recent mesocosm experiment, the organic matter in SSAs generated from the wave
490 braking of natural sea-water was monitored for 29 days after adding nutrients at the beginning of
491 the experiment during which two phytoplankton blooms occurred (Wang et al., 2015). The
492 aliphatic-rich organic matter level in the nascent SSAs was enhanced during the first bloom,
493 whereas the oxygen-rich organic matter level increased at the early period of the experiment before

494 the first bloom and remained somewhat constant thereafter, including the second bloom period.
495 The MgAla and MgFAs observed in this study are the aliphatic-rich and oxygen-rich organic
496 matters in their work, respectively, because the Raman spectra of MaAla and MgFAs are the same
497 as those for oxygen- and aliphatic-rich organic matters and the O/C atomic ratios of alanine,
498 palmitic, and stearic acids are 0.67, 0.13, and 0.11 (in their work, O/C > 0.5 for oxygen-rich organic
499 matters and <0.25 for aliphatic-rich organic matters). In this study, the summertime Antarctic SSAs
500 contain oxygen-rich organic matter, such as MgAla, whereas the wintertime SSAs contain
501 aliphatic-rich organic matter, such as MgFAs as well as oxygen-rich organic matter. The aliphatic-
502 rich organic matter was observed only during the first bloom in the mesocosm experiment, whereas
503 supermicron MgFAs-containing SSAs were encountered only in the wintertime sample S2
504 collected during no bloom event, suggesting that the chemical features of organic matter in nascent
505 SSAs cannot be correlated consistently with the phytoplankton activity. As microalgae can produce
506 more lipid and less protein under environmental stress, such as limited nutrients and low
507 temperature (Wu et al., 2011; Yu et al., 2009; Olson and Ingram, 1975), MgFAs, which were
508 biodegraded from lipid, may be observed more frequently in the wintertime oligotrophic Antarctic
509 Ocean with a lower temperature.

510

511 **4. Summary**

512 X-ray analysis of a single particle analysis showed that the supermicron summertime and
513 wintertime Antarctic samples have different elemental chemical compositions, even though all the
514 individual particles analyzed were SSAs; i.e., contents of C, O, Ca, S, and Si are more elevated,
515 whereas Cl is more depleted, for the summertime sample S1 than for the wintertime sample S2.
516 The combined application of RMS and ATR-FTIR imaging to the same individual SSAs made the
517 molecular speciation of the observed organic and inorganic species feasible. Based on qualitative
518 analysis of the chemical species present in the individual SSAs by RMS and ATR-FTIR imaging,
519 different organic species were observed in samples S1 and S2, i.e., Mg hydrate salts of alanine is
520 predominant in the S1 and S2 samples, whereas Mg salts of fatty acids mixed internally with Mg
521 hydrate salts of alanine are significant in sample S2. Although CaSO₄ are encountered significantly
522 in both samples S1 and S2, the other inorganic species, such as Na₂SO₄, NaNO₃, Mg(NO₃)₂, SiO₂,
523 and CH₃SO₃Mg were encountered more significantly in sample S1, suggesting that they reflect the
524 high phytoplankton activity in the summer.

525 In this study, there were new observations regarding the chemical compositional features
526 of nascent Antarctic SSAs and some of them need to be explained in further studies. First, although
527 just two SSA samples, having a high oceanic chlorophyll-*a* level contrast, collected in the summer
528 and winter were investigated, their chemical compositional features were clearly different in terms
529 of their chemical species and/or levels of inorganic and organic moieties. However, it is not clear
530 whether the different compositional features are due to the different sampling seasons or biological
531 activities. To answer this question, a study for overall 29 Antarctic aerosol samples collected
532 during Dec. 2011 and Sep. 2012 when the oceanic chlorophyll-*a* levels are in the range of 0.07-
533 13.38 $\mu\text{g/L}$ is underway. Second, even the supermicron SSAs were enriched significantly by
534 organic matter, and thus the effects of organic matter in supermicron SSAs need to be considered
535 more seriously in a radiative forcing model study. Third, based on the Raman and ATR-FTIR
536 measurements, the organic moieties in SSAs are believed to be present mainly as the salt forms of
537 surprisingly simple organic compounds, such as alanine and palmitic/stearic acids, which appear
538 to be the biodegraded final products from proteins and lipids, respectively, but the reason for why
539 alanine and palmitic/stearic acids are predominant as the final products is unclear. In addition, the
540 Mg hydrate salts of alanine are almost ubiquitous in both the summertime and wintertime
541 supermicron SSAs but the Mg salts of fatty acids were encountered only in the wintertime
542 supermicron SSAs, which will require further study to better understand the generation processes
543 of Antarctic SSAs.

544

545 **Acknowledgements**

546 This study was supported by Basic Science Research Programs through the National Research
547 Foundation of Korea (NRF) funded by the Ministry of Education, Science, and Technology
548 (NRF-2015R1A2A1A09003573).

549

550 **References**

551 Aarnos, H., Ylöstalo, P., and Vähätalo, A. V.: Seasonal phototransformation of dissolved organic
552 matter to ammonium, dissolved inorganic carbon, and labile substrates supporting
553

554 bacterial biomass across the Baltic Sea, *J. Geophys. Res.*, 2012, 117, G01004, doi:10.
555 1029/2010JG001633.

556 Alpert, P. A., Kilthau, W. P., Bothe, D. W., Radway, J. C., Aller, J. Y., and Knopf, D. A.: The
557 influence of marine microbial activities on aerosol production: A laboratory mesocosm
558 study, *J. Geophys. Res.*, 2015, 10.1002/2015JD023469.

559 Ault, A. P., Moffet, R. C., Baltusaitis, J., Collins, D. B., Ruppel, M. J., Cuadra-Rodriguez, L. A.,
560 Zhao, D., Guasco, T. L., Ebben, C. J., Geiger, F. M., Bertram, T. H., Prather, K. A., and
561 Grassian, V. H.: Size-Dependent Changes in Sea Spray Aerosol Composition and
562 Properties with Different Seawater Conditions, *Environ. Sci. Technol.*, 2013a, 47, 5603–
563 5612.

564 Ault, A. P., Zhao, D., Ebben, C. J., Tauber, M. J., Geiger, F. M., Prather, K. A., and Grassian, V.
565 H.: Raman microspectroscopy and vibrational sum frequency generation spectroscopy as
566 probes of the bulk and surface compositions of size-resolved sea spray aerosol particles,
567 *Phys.Chem. Chem. Phys.*, 2013b, 15, 6206-6212.

568 Bates, T. S., Quinn, P. K., Frossard, A. A., Russell, L. M., Hakala, J., Petäjä, T., Kulmala, M.,
569 Covert, D. S., Cappa, C. D., Li, S. M., Hayden, K. L., Nuaaman, I., McLaren, R., Massoli,
570 P., Canagaratna, M. R., Onasch, T. B., Sueper, D., Worsnop, D. R., and Keene, W. C.:
571 Measurements of ocean derived aerosol off the coast of California, *J. Geophys. Res.:*
572 *Atmos.* 2012, 117, D00V15.

573 Biancato, D., Ceccato, D., Chiminello, F., and Mittner, P.: Micro-PIXE and principal component
574 analysis in a study of internal mixing phenomena in Antarctic coastal aerosol, *Nucl. Instr.*
575 *Meth. Phys. Res. B*, 2006, 249, 561-565.

576 Carlucci, A. F., Hartwig, E. O., and Bowes, P. M.: Biological production of nitrite in seawater, *Mar.*
577 *Biol.*, 1970, 7, 161-166.

578 de Leeuw, G., Andreas, E' L', Angelova, M. D., Fairall, C. W., Lewis, E. R., O'Dowd, C., Schulz,
579 M., and Schwartz, S. E.: Production flux of sea spray aerosol, *Rev. Geophys.*, 2011, 49,
580 RG2001, doi:10.1029/2010RG000349.

581 Dittmar, T., Fitznar, H. P., and Kattner, G.: Origin and biogeochemical cycling of organic nitrogen
582 in the eastern Arctic Ocean as evident from D- and L-amino acids. *Geochim. Cosmochim.*
583 *Acta*, 2001, 65, 4103–4114.

584 Eom, H.-J., Jung, H.-J., Sobanska, S., Chung, S.-G., Son, Y.-S., Kim, J.-C., Sunwoo, Y., and Ro,

585 C.-U.: Iron speciation of airborne subway particles by the combined use of energy
586 dispersive electron probe X-ray microanalysis and Raman microspectrometry, *Anal.*
587 *Chem.*, 2013, 85, 10424-10431.

588 Gaston, C. J., Pratt, K. A., Qin, X., and Prather, K. A.: Real-time detection and mixing state of
589 methanesulfonate in single particles at an inland urban location during a phytoplankton
590 bloom, *Environ. Sci. Technol.*, 2010, 44, 1566–1572.

591 Gouadec, G. and Colombari, P.: Raman Spectroscopy of Nanomaterials: How Spectra Relate to
592 Disorder, Particle Size and Mechanical Properties, *Prog. Cryst. Growth Charact. Mater.*,
593 2007, 53, 1–56.

594 Gupta, D., Eom, H.-J., Cho, H.-R., and Ro, C.-U.: Hygroscopic behavior of NaCl–MgCl₂ mixture
595 particles as nascent sea-spray aerosol surrogates and observation of efflorescence during
596 humidification, *Atmos. Chem. Phys.*, 2015, 15, 11273-11290.

597 Hara, K., Osada, K., Kido, M., Matsunaga, K., Iwasaka, Y., Hashida, G., and Yamanouchi, T.:
598 Variations of constituents of individual sea-salt particles at Syowa station, Antarctica,
599 *Tellus*, 2005, 57B, 230-246.

600 Hara, K., Iwasaka, Y., Wada, M., Ihara, T., Shiba, H., Osada, K., and Yamanouchi, T.: Aerosol
601 constituents and their spatial distribution in the free troposphere of coastal Antarctic
602 regions, *J. Geophys. Res.*, 2006, 111, D15216.

603 Hara, K., Osada, K., Yabuki, M., and Yamanouchi, T.: Seasonal variation of fractionated sea-salt
604 particles on the Antarctic coast, *Geophys. Res. Lett.*, 2012, 39, L18801.

605 Hara, K., Osada, K., and Yamanouchi, T.: Tethered balloon-borne aerosol measurements: seasonal
606 and vertical variations of aerosol constituents over Syowa Station, Antarctica, *Atmos.*
607 *Chem. Phys.*, 2013, 13, 9199-9139.

608 Hara, K., Nakazawa, F., Fujita, S., Fukui, K., Enomoto, H., and Sugiyama, S.: Horizontal
609 distributions of aerosol constituents and their mixing states in Antarctica during the JASE
610 traverse, *Atmos. Chem. Phys.*, 2014, 14, 10211-10230.

611 Haynes, W. M.: *CRC Handbook of Chemistry and Physics*, 96th Edition, CRC Press, 2015, pp.
612 14-18.

613 Hovanec, T. A. and DeLong, E. F.: Comparative Analysis of Nitrifying Bacteria Associated with
614 Freshwater and Marine Aquaria, *Appl. Environ. Microb.*, 1996, 62(8), 2888-2896.

615 Hu, Q.-H., Xie, Z.-Q., Wang, X.-M., Kang, H., He, Q.-F., and Zhang, P.: Secondary organic

616 aerosols over oceans via oxidation of isoprene and monoterpenes from Arctic to Antarctic,
617 Sci. Rep., 2013, 3, 2280.

618 Jung, H.-J., Eom, H.-J., Kang, H.-W., Moreau, M., Sobanska, S., and Ro, C.-U.: Combined use of
619 quantitative ED-EPMA, Raman microspectrometry, and ATR-FTIR imaging techniques
620 for the analysis of individual particles, *Analyst*, 2014, 139, 3949-3960.

621 Kerminen, V.-M., Teinilä, K., and Hillamo, R.: Chemistry of sea-salt particles in the summer
622 Antarctic atmosphere, *Atmos. Environ.*, 2000, 34, 2817–2825.

623 Kitidis, V., Uher, G., Upstill-Goddard, R. C., Mantoura, R. F. C., Spyres, G., and Woodward, E.
624 M. S.: Photochemical production of ammonium in the oligotrophic Cyprus Gyre (Eastern
625 Mediterranean), *Biogeosciences*, 2006, 3, 439–449.

626 Laskina, O.: Physicochemical properties of mineral dust and sea spray aerosols, Ph. D. thesis, 2015,
627 129-149.

628 Lee, S. H., Joo, H. M., Joo, H., Kim, B. K., Song, H. J., Jeon, M., and Kang, S.-H.: Large
629 contribution of small phytoplankton at Marian Cove, King George Island, Antarctica,
630 based on long-term monitoring from 1996 to 2008, *Polar Biol.*, 2015, 38, 207-220.

631 Litchman, E. and Klausmeier, C. A.: Trait-Based Community Ecology of Phytoplankton, *Annu.*
632 *Rev. Ecol. Evol. Syst.*, 2008, 39, 615-639.

633 Lutz, H. D. and Haeuseler, H.: Infrared and Raman spectroscopy in inorganic solids research, *J.*
634 *Mol. Struct.*, 1999, 511–512, 69–75.

635 Maskey, S., Geng, H., Song, Y.-C., Hwang, H., Yoon, Y.-J., Ahn, K.-H., and Ro, C.-U.: Single-
636 Particle Characterization of Summertime Antarctic Aerosols Collected at King George
637 Island Using Quantitative Energy-Dispersive Electron Probe X-ray Microanalysis and
638 Attenuated Total Reflection Fourier Transform-Infrared Imaging Techniques, *Environ. Sci.*
639 *Technol.*, 2011, 45, 6275–6282.

640 O’Dowd, C. D., Facchini, M. C., Cavalli, F., Ceburnis, D., Mircea, M., Decesari, S., Fuzzi, S.,
641 Yoon, Y. J., and Putaud, J.-P.: Biogenically driven organic contribution to marine aerosol,
642 *Nature*, 2004, 431, 676-680.

643 Olson, G. J. and Ingram, L. O.: Effects of temperature and nutritional changes on the fatty acids
644 of *Agmenellum quadruplicatum*, *J. Bacteriol.*, 1975, 124, 373-379.

645 Ogawa, H. and Tanoue, E.: Dissolved Organic Matter in Oceanic Waters, *J. Oceanogr.*, 2003, 59,
646 129-147.

647 Paulot, F., Jacob, D. J., Johnson, M. T., Bell, T. G., Baker, A. R., Keene, W. C., Lima, I. D., Doney,
648 S. C., and Stock, C. A.: Global oceanic emission of ammonia: Constraints from seawater
649 and atmospheric observations, *Global Biogeochem. Cycles*, 29, 1165–1178.

650 Prather, K. A., Bertram, T. H., Grassian, V. H., Deane, G. B., Stokes, M. D., DeMott, P. J.,
651 Aluwihare, L. I., Palenik, B. P., Azam, F., Seinfeld, J. H., Moffet, R. C., Molina, M. J.,
652 Cappa, C. D., Geiger, F. M., Roberts, G. C., Russell, L. M., Ault, A. P., Baltrusaitis, J.,
653 Collins, D. B., Corrigan, C. E., Cuadra-Rodriguez, L. A., Ebben, C. J., Forestieri, S. D.,
654 Guasco, T. L., Hersey, S. P., Kim, M. J., Lambert, W. F., Modini, R. L., Mui, W., Pedler,
655 B. E., Ruppel, M. J., Ryder, O. S., Schoepp, N. G., Sullivan, R. C., and Zhao, D.: Bringing
656 the ocean into the laboratory to probe the chemical complexity of sea spray aerosol, *Proc.*
657 *Natl. Acad. Sci. USA.*, 2013, v110, 19, 7550–7555.

658 Préndez, M., Wachter, J., Vega, C., Flocchini, R. G., Wakayabashi, P., and Morales, J. R.: PM_{2.5}
659 aerosols collected in the Antarctic Peninsula with a solar powered sampler during austral
660 summer periods, *Atmos. Environ.*, 2009, 43, 5575–5578.

661 Preunkert, S., Jourdain, B., Legrand, M., Udisti, R., Becagli, S., and Cerri, O.: Seasonality of sulfur
662 species (dimethyl sulfide, sulfate, and methanesulfonate) in Antarctica: Inland versus
663 coastal regions, *J. Geophys. Res.*, 2008, 113, D15302

664 Quinn, P. K., Bates, T. S., Schulz, K. S., Coffman, D. J., Frossard, A. A., Russell, L. M., Keene,
665 W. C., and Kieber, D. J.: Contribution of sea surface carbon pool to organic matter
666 enrichment in sea spray aerosol, *Nat. Geosci.*, 2014, 7, 228–232.

667 Quinn, P. K., Collins, D. B., Grassian, V. H., and Prather, K. A.: Chemistry and Related Properties
668 of Freshly Emitted Sea Spray Aerosol, *Chem. Rev.*, 2015, 115, 4383–4399.

669 Rain-Franco, A., Muñoz, C., Fernandez, C.: Ammonium Production off Central Chile (36°S) by
670 Photodegradation of Phytoplankton-Derived and Marine Dissolved Organic Matter, *Plos*
671 *One*, 2014, 26, 9(6), e100224, doi:10.1371/journal.pone.0100224.

672 Rinaldi, M., Decesari, S., Finessi, E., Giulianelli, L., Carbone, C., Fuzzi, S., O’Dowd, C. D.,
673 Ceburnis, D., and Facchini, M. C.: Primary and Secondary Organic Marine Aerosol and
674 Oceanic Biological Activity: Recent Results and New Perspectives for Future Studies,
675 *Adv. Meteorol.*, 2010, 310682, 1-10.

676 Ro, C.-U., Osán, J., Szalóki, I., de Hoog, J., Worobiec, A., and Van Grieken, R.: A Monte Carlo
677 program for quantitative electron-induced X-ray analysis of individual particles, *Anal.*

678 Chem., 2003, 75, 851–859.

679 Ro, C.-U., Hwang, H., Kim, H., Chun, Y., and Van Grieken, R.: Single-particle characterization of
680 four “Asian dust” samples collected in Korea, using low-Z particle electron probe X-ray
681 microanalysis, *Environ. Sci. Technol.*, 2005, 39, 1409–1419.

682 Ro, C.-U., Osán, J., and Van Grieken, R.: Determination of low-Z elements in individual
683 environmental particles using windowless EPMA, *Anal. Chem.*, 1999, 71, 1521–1528.

684 Schindelholz, E., Risteen, B. E., and Kelly, R. G.: Effect of Relative Humidity on Corrosion of
685 Steel under Sea Salt Aerosol Proxies, *J. Electrochem. Soc.*, 2014, 161 (10), C460-470.

686 Schloss, I. R., Wasilowska, A., Dumont, D., Almandoz, G. O., Hernando, M. P., Michaud-
687 Tremblay, C.-A., Saravia, L., Rzepecki, M., Monien, P., Monien, D., Kopczyńska, E. E.,
688 Bers, A. V., Ferreyra, G. A.: On the phytoplankton bloom in coastal waters of southern
689 King George Island (Antarctica) in January 2010: An exceptional feature?, *Limnol.*
690 *Oceanogr.*, 2014, 59(1), 195-210.

691 Shebanova, O. N. and Lazor, P. J.: Raman spectroscopic study of magnetite (FeFe_2O_4): a new
692 assignment for the vibrational spectrum, *Solid State Chem.*, 2003, 174, 424–430.

693 Smith, J. M., Chavez, F. P., and Francis, C. A.: Ammonium Uptake by Phytoplankton Regulates
694 Nitrification in the Sunlit Ocean, *Plos One*, 24, 9(9), e108173. doi:10.1371/journal.pone.
695 0108173.

696 Sobanska, S., Hwang, H., Choël, M., Jung, H.-J., Eom, H.-J., Kim, H., Barbillat, J., and Ro, C.-U.:
697 Investigation of the Chemical Mixing State of Individual Asian Dust Particles by the
698 Combined Use of Electron Probe X-ray Microanalysis and Raman Microspectrometry,
699 *Anal. Chem.*, 2012, 84, 3145–3154.

700 Song, Y.-C., Ryu, J., Malek, M. A., Jung, H.-J., and Ro, C.-U.: Chemical speciation of individual
701 airborne particles by the combined use of quantitative energy-dispersive electron probe
702 X-ray microanalysis and attenuated total reflection Fourier transform-infrared imaging
703 techniques, *Anal. Chem.*, 2010, 82, 7987–7998.

704 Song, Y.-C., Eom, H.-J., Jung, H.-J., Malek, M. A., Kim, H. K., Geng, H., and Ro, C.-U.:
705 Investigation of aged Asian dust particles by the combined use of quantitative ED-
706 EPMA and ATR-FTIR imaging, *Atmos. Chem. Phys.*, 2013, 13, 3463-3480.

707 Tolar, B. B., Ross, M. J., Wallsgrove, N. J., Liu, Q., Aluwihare, L. I., Popp, B. N., and Hollibaugh,
708 J. T.: Contribution of ammonia oxidation to chemoautotrophy in Antarctic coastal waters,
709 ISME. J., 2016, 1-15.

710 Van Dalen, G., Heussen, P. C. M., Den Adel, R., and Hoeve, R. B. J.: Attenuated total internal
711 reflection infrared microscopy of multilayer plastic packaging foils, *Appl. Spectrosc.*,
712 2007, 61, 593–602.

713 Vekemans, B., Janssens, K., Vincze, L., Adams, F., and Van Espen, P.: Analysis of X-ray spectra
714 by iterative least squares (AXIL): New developments, *X-Ray Spectrom.*, 1994, 23, 278–
715 285.

716 Wagenbach, D., Ducroz, F., Mulvaney, R., Keck, L., Minikin, A., Legrand, M., Hall, J. S., and
717 Wolff, E. W.: Sea-salt aerosol in coastal Antarctic regions, *J. Geophys. Res.*, 1998, 103,
718 10961–10974.

719 Wang, X., Sultana, C. M., Trueblood, J., Hill, T. C. J., Malfatti, F., Lee, C., Laskina, O., Moore, K.
720 A., Beall, C. M., McCluskey, C. S., Cornwell, G. C., Zhou, Y., Cox, J. L., Pendergraft, M.
721 A., Santander, M. V., Bertram, T. H., Cappa, C. D., Azam, F., DeMott, P. J., Grassian, V.
722 H., and Prather, K. A.: Microbial Control of Sea Spray Aerosol Composition: A Tale of
723 Two Blooms, *ACS Cent. Sci.*, 2015, 1, 124–131.

724 Wu, H., Volponi, J. V., Oliver, A. E., Parikh, A. N., Simmons, B. A., and Singh, S.: In vivo
725 lipidomics using single-cell Raman spectroscopy, *Proc. Natl. Acad. Sci. USA.*, 2011, 108,
726 3809-3814.

727 Xiao, H.-S., Dong, J.-L., Wang, L.-Y., Zhao, L.-J., Wang, F., and Zhang, Y.-H.: Spatially resolved
728 micro-Raman observation on the phase separation of effloresced sea salt droplets, *Environ.*
729 *Sci. Technol.*, 2008, 42, 8698-8702.

730 Xie, H., Bélanger, S., Song, G., Benner, R., Taalba, A., Blais, M., Tremblay, J.-É., and Babin, M.:
731 Photoproduction of ammonium in the southeastern Beaufort Sea and its biogeochemical
732 implications, *Biogeosciences*, 2012, 9, 3047–3061.

733 Yan, J., Asami, T., and Kuriyagawa, T.: Nondestructive measurement of machining-induced
734 amorphous layers in single-crystal silicon by laser micro-Raman spectroscopy, *Precision*
735 *Eng.*, 2008, 32, 186–195.

736 Yu, E. T., Zendejas, F. J., Lane, P. D., Gaucher, S., Simmons, B. A., and Lane, T. W.:
737 Triacylglycerol accumulation and profiling in the model diatoms *Thalassiosira*

738 *pseudonana* and *Phaeodactylum tricornutum* (Baccilariophyceae) during starvation, J.
739 *Appl. Phycol.*, 2009, 21, 669-681.

Table 1. Atomic concentration ratios of the chemical elements to Na for individual particles in the summertime and wintertime PM_{2.5-10} and PM_{1.0-2.5} fractions.

sample		Summertime sample S1		Wintertime sample S2	
size fraction		PM _{1.0-2.5} (stage 3)	PM _{2.5-10} (stage 2)	PM _{1.0-2.5} (stage 3)	PM _{2.5-10} (stage 2)
number of particles analyzed		146	148	154	156
average size (μm)		2.0 (±0.6)	2.9 (±1.5)	1.7 (±0.8)	3.2 (±1.5)
Elemental ratios	Sea-water ratios in atomic conc.*	Atomic concentration ratios			
[C]/[Na]	0.01	1.12 (±0.35)	0.87 (±0.33)	0.83 (±0.33)	0.70 (±0.24)
[O]/[Na]	114.03**	0.71 (±0.23)	0.77 (±0.25)	0.66 (±0.22)	0.68 (±0.24)
[Mg]/[Na]	0.11	0.09 (±0.02)	0.11 (±0.04)	0.11 (±0.03)	0.10 (±0.03)
[Cl]/[Na]	1.16	0.98 (±0.05)	1.01 (±0.05)	1.02 (±0.10)	1.04 (±0.04)
[K]/[Na]	0.02	0.02 (±0.01)	0.02 (±0.01)	0.01 (±0.01)	0.02 (±0.01)
[S]/[Na]	0.06	0.065 (±0.015)	0.070 (±0.019)	0.058 (±0.013)	0.059 (±0.016)
[Ca]/[Na]	0.02	0.022 (±0.009)	0.027 (±0.011)	0.018 (±0.029)	0.023 (±0.012)
[Si]/[Na]	0.00	0.03 (±0.02)	0.01 (±0.01)	0.00	0.00
Encountering frequency of particles with [S]/[Na] > 0.06		52.7%	69.7%	43.8%	41.9%
Encountering frequency of particles with [Ca]/[Na] > 0.02		48.4%	69.7%	31.5%	48.6%
Encountering frequency of particles with [Si]/[Na] > 0.00		93.4%	47.5%	-	-
* refs. : Haynes, W. M., 2015; Hara et al., 2005					
** [O]/[Na] value for sea-water is not meaningful as H ₂ O content in sea-water is considered.					

Table 2. Relative encountering frequencies (in %) of the organic and inorganic species of individual summertime and wintertime SSAs.

Organic salt group	sample	Summertime sample S1		Wintertime sample S2	
	size fraction	PM _{1.0-2.5} (stage 3)	PM _{2.5-10} (stage 2)	PM _{1.0-2.5} (stage 3)	PM _{2.5-10} (stage 2)
	number of particles analyzed	58	70	64	62
containing Mg hydrate salts of alanine (MgAla)	<i>overall</i>	100.0	100.0	76.6	33.9
	with CaSO ₄	98.3	92.9	76.6	29.0
	with Na ₂ SO ₄	98.3	88.6	18.8	4.8
	with Mg(NO ₃) ₂	51.7	77.1	32.8	22.6
	with NH ₄ NO ₃	3.4	-	6.3	-
	with NaNO ₃	-	38.6	7.8	14.5
	with Mg methanesulfonate	3.4			
	with SiO ₂	46.6	27.1	6.3	1.6
containing Mg salts of fatty acids (MgFAs)	<i>overall</i>			1.6	11.3
	with CaSO ₄			1.6	6.4
	with Mg(NO ₃) ₂			1.6	3.2
containing both MgAla and MgFAs	<i>overall</i>			21.9	54.8
	with CaSO ₄			20.3	53.2
	with Na ₂ SO ₄			7.8	3.2
	with Mg(NO ₃) ₂			9.4	50.0
	with NH ₄ NO ₃			1.6	-
	with NaNO ₃			4.7	12.9
	with SiO ₂			1.6	1.6

Figure 1. Typical secondary electron images (SEIs) of aerosol particles on stages 2 of the austral (a) summertime and (b) wintertime samples collected at King Sejong station, Antarctica.



Figure 2. Secondary electron, molecular Raman map, and elemental X-ray map (overlaid on SEIs) images of two typical (a) summertime and (b) wintertime SSAs.

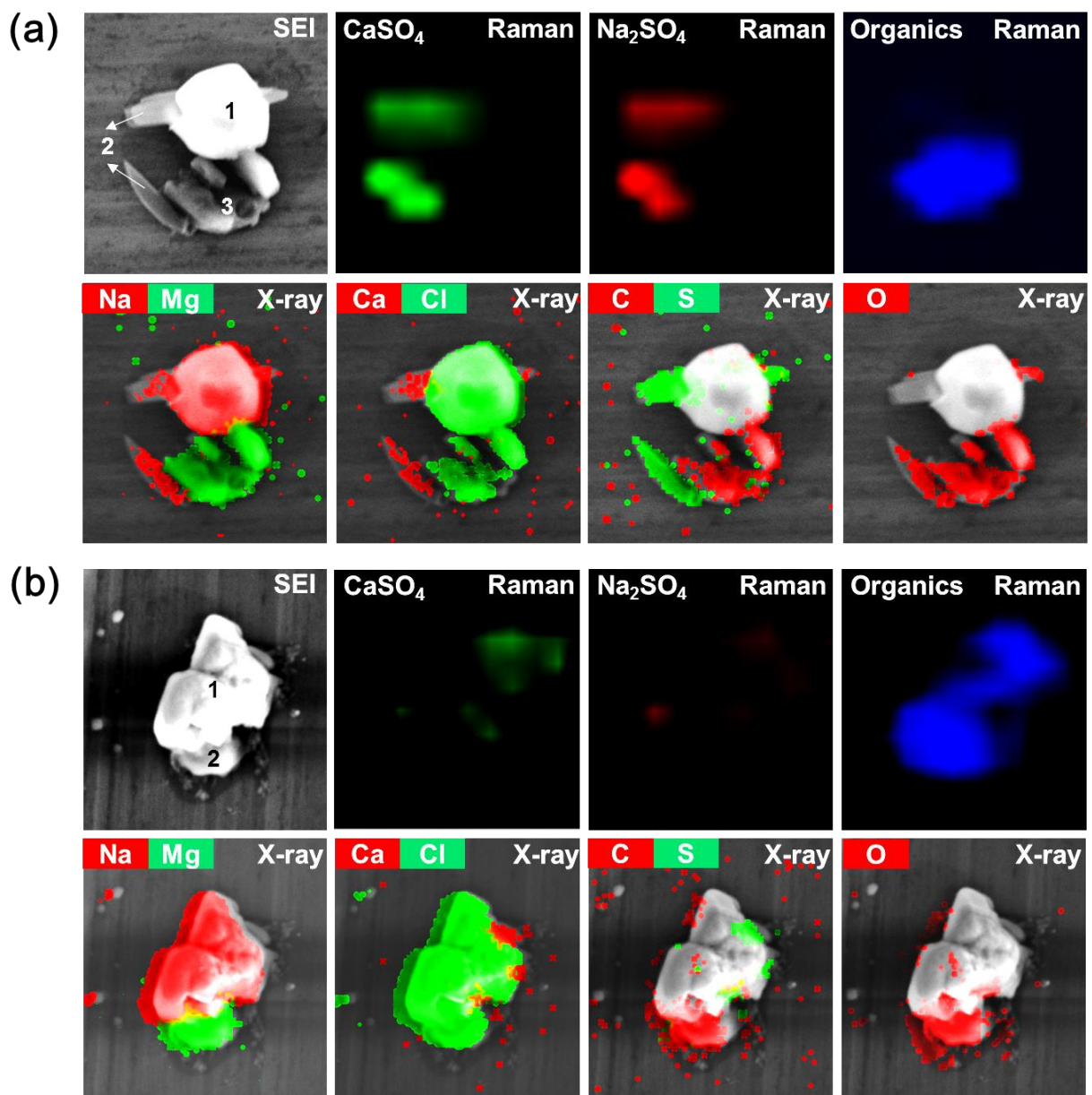


Figure 3. X-ray spectra and elemental atomic concentrations (in atomic %) of (a) the summertime and (b) wintertime SSA particles shown in Figure 2.

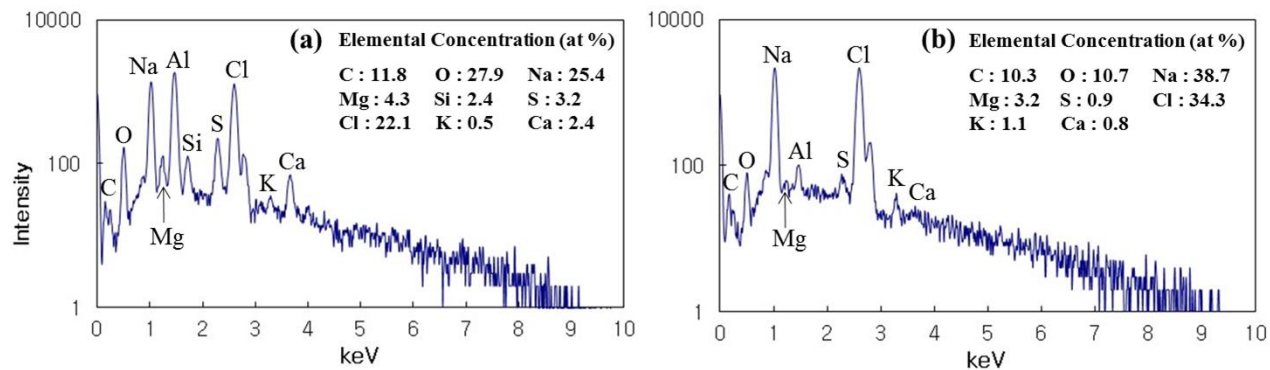


Figure 4. Raman and ATR-FTIR spectra of two typical individual summertime SSAs. The ATR-FTIR data from the 2200–2390 cm^{-1} region, where the atmospheric CO_2 peaks are present, were deleted for clarity.

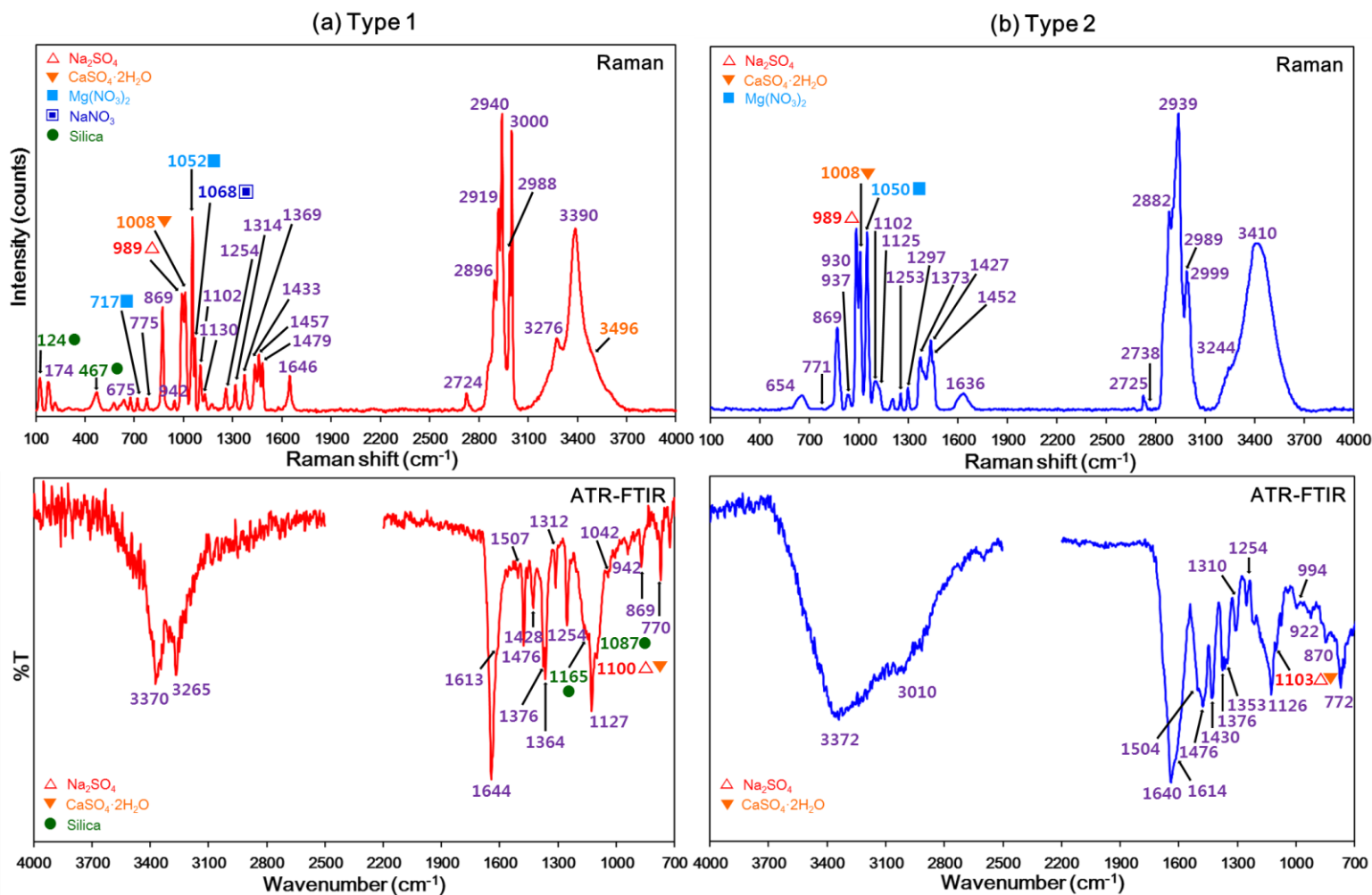


Figure 5. Raman and ATR-FTIR spectra of two typical individual wintertime SSAs. The ATR-FTIR data from the 2200–2390 cm^{-1} region, where atmospheric CO_2 peaks are present, were deleted for clarity.

